

Features of Gaia DR3 Spectroscopic Binaries

I. Tidal circularization of Main-Sequence Stars

Dolev Bashi,^{*} Tsevi Mazeh and Simchon Faigler

School of Physics and Astronomy, Tel Aviv University, Tel Aviv, 6997801, Israel

Accepted XXX. Received YYY; in original form ZZZ

ABSTRACT

Previous studies pointed out that many observed samples of short-period binaries display a cutoff period, P_{cut} , such that almost all binaries with periods shorter than P_{cut} have circular orbits. This feature is probably due to long-term circularization processes induced by tidal interaction between the two stars of each binary. It seemed as if coeval main-sequence (MS) samples of open clusters display P_{cut} that depends on the sample age. Using the unprecedentedly large sample of MS spectroscopic orbits recently released by *Gaia* we have found that the P_{cut} does not depend on the stellar age but, instead, varies with stellar temperature, decreasing *linearly* from 6.5 day at $T_{\text{eff}} \sim 5700$ K to ~ 2.5 day at 6800 K. P_{cut} was derived by a new algorithm that relied on clear upper envelopes displayed in the period-eccentricity diagrams. Our P_{cut} determines both the border between the circular and eccentric binaries and the location of the upper envelope. The results are inconsistent with the theory which assumes circularization occurs during the stellar MS phase, a theory that was adopted by many studies. The circularization has probably taken place at the pre-main-sequence phase, as suggested already in 1989 by Zahn and Bouchet, and later by Khaluillin and Khaluillina in 2011. Our results suggest that the weak dependence of P_{cut} on the cluster age is not significant, and/or might be due to the different temperatures of the samples. If indeed true, this has far-reaching implications for the theory of binary and exoplanet circularization, synchronization, and alignment.

Key words: binaries: close – binaries: spectroscopic – methods: statistical

1 INTRODUCTION

The *Gaia* latest release of Non-Single Star catalogs ([Gaia Collaboration et al. 2022](#), hereafter *NSS*) includes the orbits of 181 327 single-lined spectroscopic binaries (SB1), based on the radial velocities obtained by the space-mission RVS spectrograph ([Recio-Blanco et al. 2022](#); [Blomme et al. 2022](#); [Katz et al. 2022](#)). The *NSS* SB1 catalog is substantially larger than any previously-known catalog, and therefore is a gold mine for investigating the statistical features of short-period binaries (e.g., [Duquennoy & Mayor 1991](#); [Duchêne & Kraus 2013](#); [Torres et al. 2021](#)), like the frequency of binaries as a function of the primary mass ([Raghavan et al. 2010](#); [Troup et al. 2016](#); [Moe & Di Stefano 2017](#)) and mass-ratio distributions (e.g., [Mazeh & Goldberg 1992](#); [Boffin 2012, 2015](#); [Shahaf et al. 2017](#)).

This work utilizes the *NSS* catalog to follow the tidal circularization of short-period binaries. Based on theoretical work, we expect short-period binaries ($\lesssim 3 - 10$ day) to be circularized (e.g., [Kopal 1956](#); [Mayor & Mermilliod 1984](#); [Giuricin et al. 1984](#); [Zahn 2008](#)) by the tidal interaction between the two components, whose strength is a strong function of the binary separation and primary radius (e.g., [Zahn 1975, 1977, 1989](#)). This expectation caused [Gaia Collaboration et al. \(2022\)](#) to question the validity of the very short-period binaries, with periods shorter than one day and large eccentricities. We,

therefore, rely on the work of [Bashi et al. \(2022\)](#), who confronted the *NSS* SB1 orbits with the LAMOST and GALAH RV databases, and constructed a clean sample of 91 740 *Gaia* SB1 orbits. This sample is the basis of our period-eccentricity relation.

Observational evidence for tidal circularization, based on small samples of spectroscopic binaries, was already pointed out by [Mayor & Mermilliod \(1984\)](#) and [Mathieu & Mazeh \(1988\)](#). They considered samples of coeval spectroscopic binaries and showed that each sample displays a circularization "cutoff period", P_{cut} , out to which most binaries have circular orbits, while most binaries of longer periods have eccentric orbits (see also [Mathieu et al. 2004](#)). The idea behind the cutoff period is the strong dependence of the tidal interaction on the binary separation and therefore on the binary period. Binaries with periods longer than P_{cut} were not circularized, keeping their primordial eccentricity. In this model, coeval binary samples should display a discontinuity jump of the eccentricity at P_{cut} , which should depend on the sample age — the older the sample the longer P_{cut} (e.g., [Mathieu & Mazeh 1988](#); [Mathieu et al. 2004](#); [Geller et al. 2008, 2010](#); [Geller & Mathieu 2012](#); [Nine et al. 2020](#); [Geller et al. 2021](#); [Zanazzi 2022](#)).

Another avenue to observationally study the tidal circularization was taken by [North & Zahn \(2003\)](#) and [Mazeh et al. \(2006\)](#), and recently by the seminal works of [Van Eylen et al. \(2016\)](#) and [Justesen & Albrecht \(2021\)](#); see also [Zanazzi \(2022\)](#). They considered samples of eclipsing binaries (EB) — those of OGLE LMC ([Wyrzykowski](#)

^{*} E-mail: dolevbashi@gmail.com

et al. 2003), *Kepler* (Slawson et al. 2011) and *TESS* (Ricker et al. 2015), obtaining the projected eccentricity of those binaries from the timing of the secondary eclipse (Sterne 1940). These studies used the fact that a light curve of an EB allows for deriving the stellar radii relative to the binary separation, and therefore the ratio between the sum of radii of the two components and the binary separation, a ratio that directly determines the tidal circularization effectiveness (North & Zahn 2003). Thus, the analysis of EB samples provides a cutoff ratio that divides circular from eccentric orbits. Justesen & Albrecht (2021) derived the cutoff ratio for binaries with different temperatures. Such a ratio is not available for spectroscopic binaries, and therefore one can study only the cutoff period.

When studying spectroscopic samples, Meibom & Mathieu (2005) suggested a more composite approach for determining the cutoff period of a binary sample. They considered the eccentricity as a piecewise function of the period, P , with zero eccentricity for $P < P_{\text{cut}}$ and a smooth rising asymptotic function that goes up to eccentricity close to unity for $P > P_{\text{cut}}$. The idea behind the Meibom & Mathieu (2005) approach is that even binaries with $P > P_{\text{cut}}$ are subject to the circularization processes that decreased the primordial eccentricity, but were not strong enough to make the orbit circular. The reduced eccentricities of those binaries depend on the primordial orbital period and eccentricity and the strength of the tidal interaction. The asymptotic function reflects the present characteristics of the whole binary sample and not only the very short-period circularized binaries (see this approach applied, for example, by Nine et al. (2020) and with a different version by Zanazzi (2022)).

Following Mazeh (2008) (see also, for example, Pourbaix et al. 2007) we consider here a piece-wise asymptotic function that presents an upper envelope for the eccentricity as a function of the period for a given sample. The function marks the edge of the populated part of the period-eccentricity plane. For a given period, there are almost no binaries with eccentricity larger than the asymptotic-function value at this period, while there is a high probability of finding binaries with eccentricities smaller than that value. In short, we view the period-eccentricity diagram as divided into two regimes, separated by an upper-envelope asymptotic function. We use Mazeh et al. (2016) algorithm to find the best upper envelope by a maximum-likelihood approach, given a sample of spectroscopic binaries. Similar to Meibom & Mathieu (2005), we define the cutoff period, P_{cut} , as the period at which the upper envelope cuts the eccentricity axis, i.e., $e = 0$. In this approach, P_{cut} denotes both the border between the circular and eccentric binaries and the location of the upper-envelope base.

The large cleaned *Gaia* sample of Bashi et al. (2022) allows us to apply our technique to a few sub-samples of the *Gaia* SB1s. We concentrate on the binaries with main-sequence (MS) A-, F- and G-primaries, identified by their position on the *Gaia* Colour-Magnitude Diagram (CMD). Similar to the Justesen & Albrecht (2021) analysis, we divided the sample into temperature bins, and derived their corresponding P_{cut} independently, finding a clear dependence on the stellar temperature of each bin.

Section 2 details the *Gaia* sample used, including removing binaries with unconstrained eccentricities. Section 3 presents our algorithm to obtain the best parameters of the upper envelope, given a binary sample, and Section 4 tests our algorithm for six simulated binary samples. Section 5 presents our main result — the dependence of P_{cut} on the primary temperature of each sub-sample. Section 6 shows that the results are inconsistent with the theory which assumes circularization occurs during the stellar MS phase. Section 7 summarizes our results and discusses their possible implications.

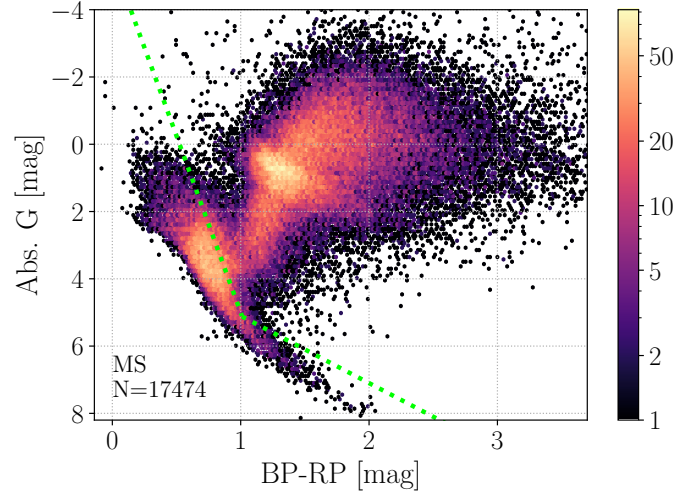


Figure 1. Colour-Magnitude Diagram (CMD) of the clean *Gaia* sample of Bashi et al. (2022) binaries. The colour scale represents the number of binaries falling into each hexagonal bin. The dashed line (see text) delineates our border of the MS binaries.

2 THE SAMPLE

We wish to study the eccentricity distribution of the *Gaia* binaries, as a function of the stellar temperature in particular. We, therefore, consider a uniform sample of binaries with unevolved primaries, of derived effective temperature, and orbits with well-constrained eccentricity. Such a reduced sample is composed in this section.

2.1 The main-sequence binaries

We first cross-matched the clean sample of Bashi et al. (2022) with the TESS Input Catalog¹ (TIC; Stassun et al. 2018; Paegert et al. 2021), yielding 89 742 SB1s. Fig. 1 shows these binaries on the *Gaia* Color-Magnitude Diagram (CMD), clearly displaying the difference between the MS and the evolved stars. To identify the MS binaries we used the limits

$$\text{MS} : \begin{cases} -5.5 + 10.5(G_{\text{BP}} - G_{\text{RP}}) < G, & \text{if } G_{\text{BP}} - G_{\text{RP}} \leq 1, \\ 3.1 + 2(G_{\text{BP}} - G_{\text{RP}}) < G, & \text{if } G_{\text{BP}} - G_{\text{RP}} > 1, \end{cases} \quad (1)$$

which left us with 17 474 binaries.

2.2 Removing orbits with unconstrained eccentricity

Fig. 2 shows the period-eccentricity (P - e) diagram for the MS-reduced sample. Two features are clearly seen:

- An upper envelope that rises from $e \sim 0.1$ at period of $P \sim 3$ day towards $e \sim 0.8$ at period of $P \sim 100$ day.
- A high concentration of binaries centered at $P \sim 5$ day and low eccentricity of ~ 0.03 .

To check which of these low eccentricities are real (see also a discussion by Bashi et al. 2022), we used here the Lucy & Sweeney (1971) approach (see also Hara et al. 2019, in the context of the eccentricity of planetary orbits), who suggested that the actual eccentricity uncertainty is larger than the one derived by the regular

¹ <https://tess.mit.edu/science/tess-input-catalogue/>

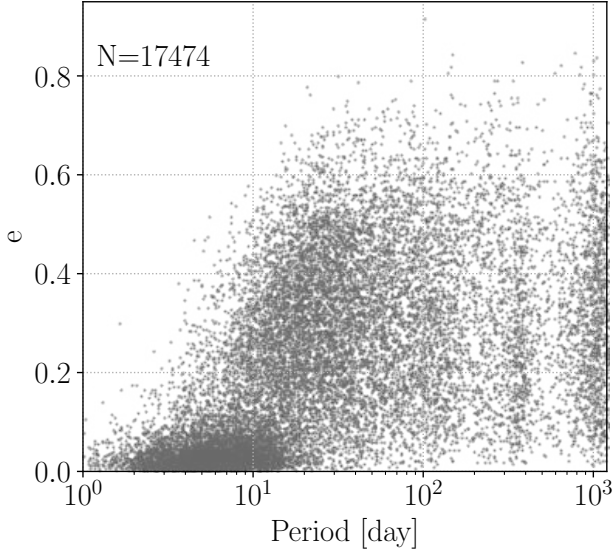


Figure 2. Period-eccentricity diagram for the cleaned MS SB1 sample.

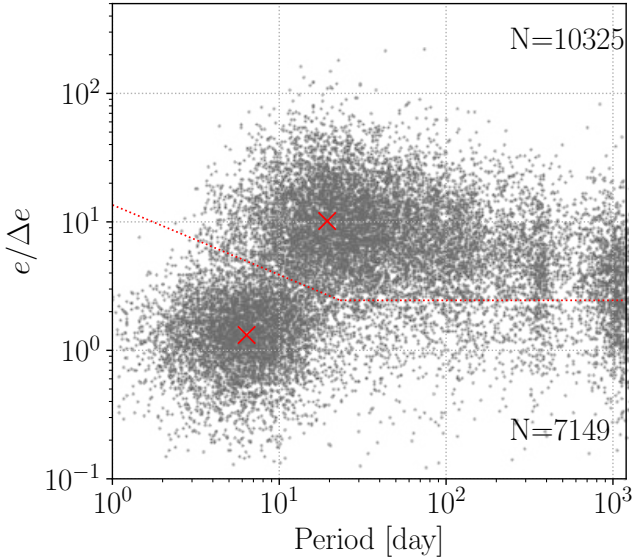


Figure 3. Ratio between the derived eccentricities and their corresponding uncertainties as a function of the orbital period. Red dashed horizontal line marks the $e/\Delta e = 2.45$ threshold of [Lucy & Sweeney \(1971\)](#).

analysis. Thus, [Lucy & Sweeney \(1971\)](#) suggested that many derived eccentricities of their time might be spurious.

We, therefore, plot in [Fig. 3](#) the ratio between the derived *Gaia* eccentricities and their corresponding uncertainties as a function of the orbital periods. Two emerging clusters can be seen for binaries with orbital periods shorter than 100 days. Using K-means clustering ([Pedregosa et al. 2011](#))², we found the center of the bottom cluster at

$(P, e/\Delta e) = (6.37, 1.32)$, while the upper-cluster center is at $(19.38, 10.15)$. Using the [Lucy & Sweeney \(1971\)](#) 5% level of significance for testing the hypothesis that $e = 0$, we found most binaries in the lower cluster to be under the threshold of $e/\Delta e = 2.45$. To define a sample of binaries with well-constrained eccentricities, we drew a line perpendicular to the line connecting the two cluster centres through the middle of the gap between the two clusters. This has left us with a sample of 10 325 binaries with at least 95% confidence for non-circular eccentricity, and 7 149 binaries with unconstrained eccentricities.

[Fig. 4](#) presents the two sub-samples. As can be clearly seen, the dense area of near-circular binaries is populated by the unconstrained eccentricity sources only.

Next, we wish to test whether the clear distinction between the two sub-samples of [Fig. 4](#) is a result of an age difference, as one might argue that the nearly circular binaries are old MS binaries that had already completed their tidal circularization. We, therefore, plot in [Fig. 5](#) the age-effective temperature dependence of each of the two sub-sample. The left panel includes a sample of 4 530 binaries with unconstrained eccentricities for which *Gaia* FLAME stellar effective temperature and age (`age_flame`) are available. Similarly, the right panel includes a sample of 6 389 sources with non-circular solutions. Overall, a strong correlation between effective temperature and age is evident in both panels, as expected for MS stars, with no apparent age difference.

In what follows, we concentrate on analysing the sub-sample of 10 325 binaries with well-constrained eccentricities, deriving the dependence of P_{cut} on the stellar temperature. We will also show that P_{cut} does not display a dependence on stellar age.

3 FITTING AN UPPER ENVELOPE TO THE PERIOD-ECCENTRICITY DIAGRAM

The right panel of [Fig. 4](#) clearly shows that the binary eccentricities do not present a clear cutoff period that separates the circular and the eccentric binaries, but, instead, show a gradual rise toward high values. Furthermore, the eccentricities are not concentrated around an upper envelope but are spread out between almost zero eccentricity and the upper bound. The figure suggests that the base of the envelope can serve as a better definition for the cutoff period. Any circularization analysis should try to account for this feature.

To better characterize the P - e diagram we define an upper envelope as

$$f(P) = \begin{cases} 1 - \left(\frac{P_{\text{cut}}}{P}\right)^{1/\tau} & P_{\text{cut}} < P, \\ 0 & P_{\text{cut}} \geq P, \end{cases} \quad (2)$$

where P_{cut} is the cutoff period (see also [Zanazzi 2022](#)) and τ is a dimensionless parameter that determines the slope of the envelope. The function gets a value of zero at P_{cut} for any value of τ , and asymptotically rises to unity as P gets substantially larger than P_{cut} . Note that the function is simple with only two free parameters — P_{cut} and τ . P_{cut} defines both the separation between the circular and eccentric orbits and the location of the upper envelope.

To get a sense of the role of τ , one can plot (see the bottom panel of [Fig. 6](#)) the analysed sample in the $(\log P, \log(1 - e))$ plane. In this plane, the upper envelope turns into a straight-line lower envelope with a slope of $-1/\tau$. Another way to follow the meaning of τ is to consider, for example, $P_{0.8}(P_{\text{cut}}, \tau)$ — the period for which the upper envelope gets the value of $e = 0.8$. It is easy to show that $P_{0.8} = 5^\tau P_{\text{cut}}$. In other words, τ measures by how much we have to

² <https://scikit-learn.org/stable/modules/generated/sklearn.cluster.KMeans.html>

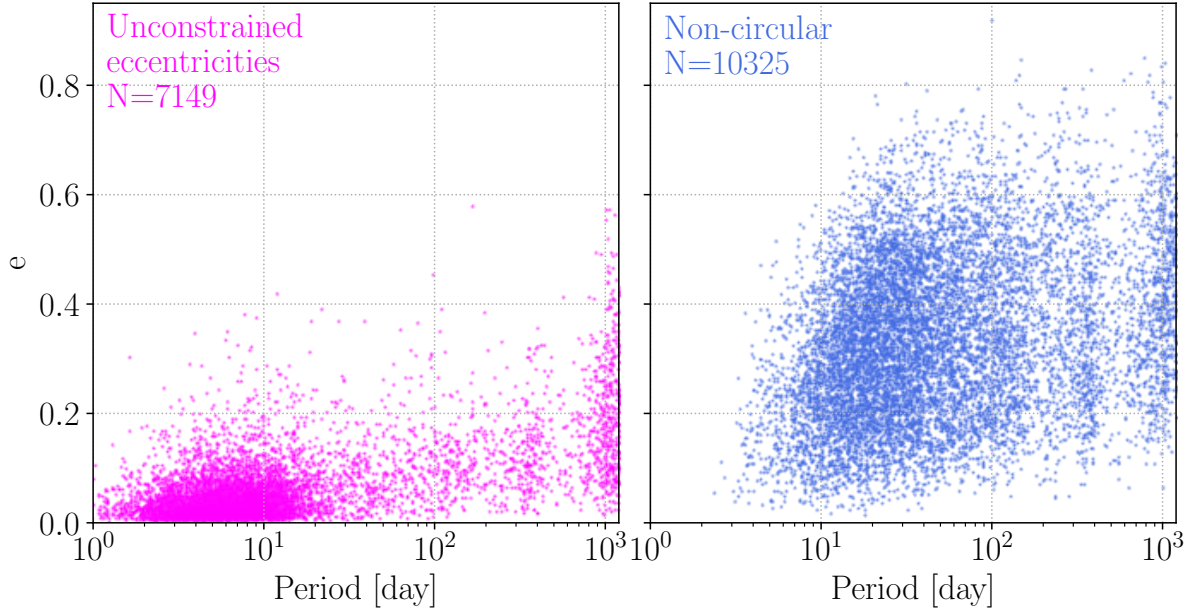


Figure 4. Period-eccentricity diagram for the cleaned SB1 sample of MS unconstrained eccentricities (left) and non-circular (right) binaries.

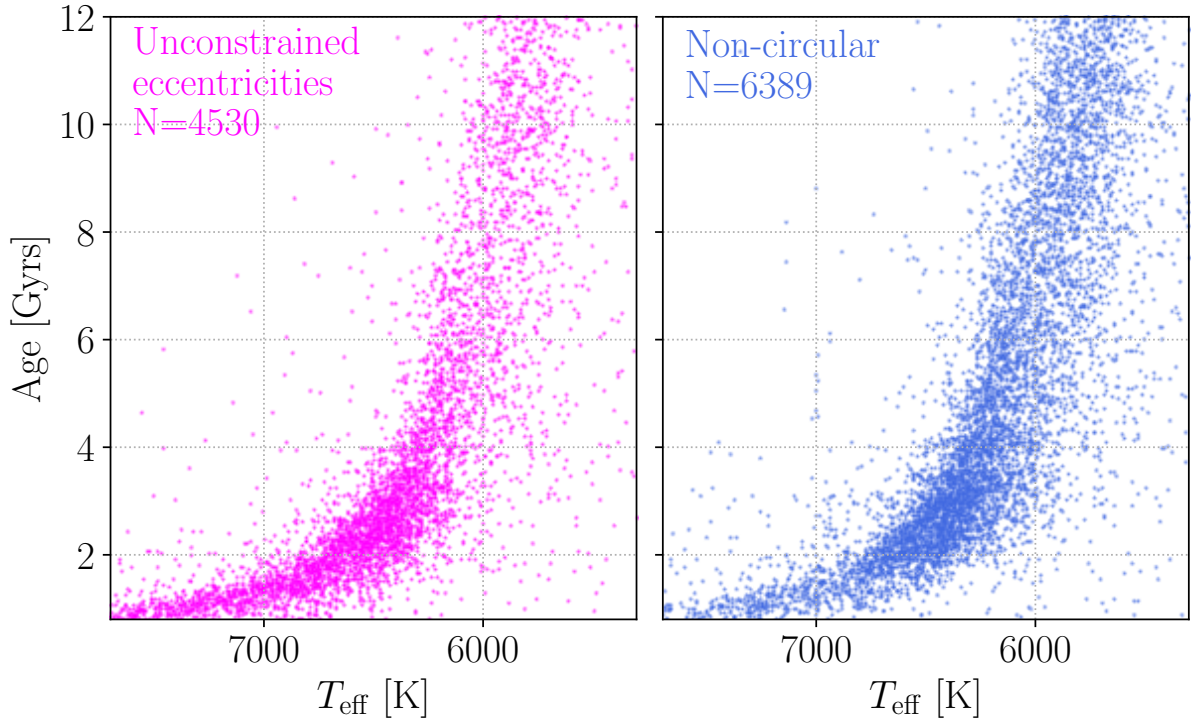


Figure 5. Stellar Age-effective temperature scatter plot of the unconstrained eccentricities sample (left) and non-circular (right) samples. A similar trend between the two parameters is evident in both panels.

increase P , relative to P_{cut} , for the upper envelope to get a value of $e = 0.8$.

We then follow [Mazeh et al. \(2016\)](#) and use a modified Fermi function to describe an assumed probability density function (PDF) of binaries above and below the upper envelope in the $(\log P, e)$ plane. The PDF converges to zero above the envelope, and to a positive constant below it. The transition region between the two parts is

along the envelope, with a width characterized by a parameter δ . The probability density at a point $(\log P, e)$ is a function of its distance $d(\log P, e; P_{\text{cut}}, \tau)$ to the envelope curve along the $\log P$ axis and can be expressed as:

$$d = \log P - \log f^{-1}(e) = \log \left[\frac{P}{P_{\text{cut}}} (1 + e)^\tau \right], \quad (3)$$

where $f^{-1}(e)$ is the inverse function of $f(P)$ defined in equation 2. The distance d is positive for points to the right and below the envelope and negative on the other side. The PDF is

$$\mathcal{F}_{\text{PDF}}(P, e; P_{\text{cut}}, \tau, \delta) = \mathcal{A} \frac{1}{1 + \exp(-d/\delta)}, \quad (4)$$

where the constant \mathcal{A} , in units of $1/[\log(P/1 \text{ day}) e]$, is defined such that the 2D integral over the $(\log P, e)$ plane, using the three parameters — $P_{\text{cut}}, \tau, \delta$, equals unity. To get a sense of this function, one can see that when $d = 0$ the PDF value is simply $\mathcal{A}/2$, while at $d = \pm\delta$ it changes between $0.27\mathcal{A}$ and $0.73\mathcal{A}$.

Obviously, the probability density function is of a statistical nature. One can find binary systems above the upper envelope, either due to erroneous measurements or invalid orbits or because of some special astrophysical circumstances, like a high primordial eccentricity or a distant faint companion that pumped eccentricity into the spectroscopic orbit (e.g., Mazeh & Shaham 1979; Mazeh 1990; Jha et al. 2000). The advantage of our approach is that for large enough samples the derivation of the envelope is only slightly sensitive to these ‘outlier’ binaries, as the fit is to the population as a whole. On the other hand, the results are not biased by the number of binaries in the sample.

For each set of parameters of the PDF — P_{cut}, τ and δ , we derive the likelihood of a given sample of N binaries, as

$$\mathcal{L} = \prod_{i=1}^N \mathcal{F}_{\text{PDF}}(P_i, e_i; P_{\text{cut}}, \tau, \delta). \quad (5)$$

where e_i and P_i are the eccentricity and period of the i -th binary.

We applied our algorithm to the sample of the *Gaia* well-constrained eccentricities discussed above, using only a reduced subsample of 4430 binaries with orbital periods shorter than 30 days. This was done because the density of the binaries with periods larger than 30 days is clearly not constant, contrary to the assumption of our algorithm. To find the upper envelope of the reduced MS sample of Fig. 4 we ran an MCMC routine with 50 walkers and 10^4 steps, with uninformative priors on the free parameters: $\log P_{\text{cut}} \sim \mathcal{U}(-1, 1)$; $\tau \sim \mathcal{U}(0, 4)$ and $\delta \sim \mathcal{U}(0.01, 0.3)$. We used the Python *emcee* package (Foreman-Mackey et al. 2013) to find the parameter values (and their uncertainties) that maximize the sample likelihood.

Fig. 6 shows our best-fit upper envelope with $P_{\text{cut}} = 4.67$ day, $\tau = 1.70$ and $\delta = 0.09$. The bottom panel of the figure displays the analyzed sample in the $(\log P, \log(1 - e))$ plane. In this plane, the upper envelope turns into a straight-line lower envelope with a slope of $-1/\tau$, showing how τ controls the slope of the upper (lower) envelope.

4 TESTING OUR ALGORITHM ON SIMULATED BINARY SAMPLES

To test our upper-envelope algorithm, we performed a simplified simulation of six binary samples with different circularization efficacy coefficients, all starting with the same flat distribution of eccentricity and log-period.

The binaries were numerically evolved with Hut (1981) (see also Terquem & Martin 2021) equations (Zahn 1975, 1977; Zahn &

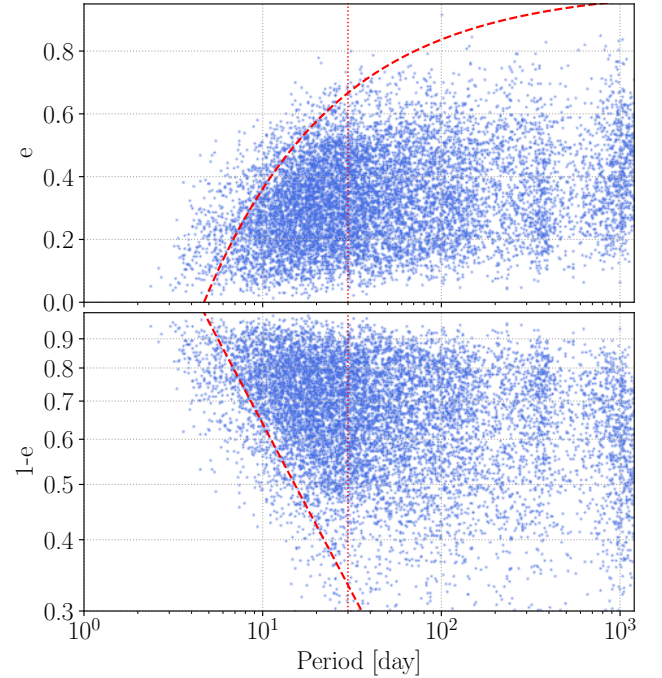


Figure 6. Top: Log period – eccentricity diagram for the cleaned SB1 sample of MS binaries, after removing orbits with unconstrained eccentricities (see text). The red dashed line marks our upper envelope best-fit model, based on binaries with an orbital period shorter than 30 days, marked by a vertical dotted line (see Section 3 for more details). Bottom: The same sample plotted on the $(\log P, \log(1 - e))$ plane. The same upper envelope is now a straight-line lower envelope, with a slope of τ .

Bouchet 1989; Zahn 1989) for stars with convective envelopes:

$$\begin{aligned} \frac{de}{dt} = & -\frac{18}{7} B \left(\frac{P}{1 \text{ day}} \right)^{-16/3} \frac{e}{(1 - e^2)^{13/2}} \left[1 + \frac{15}{4} e^2 + \frac{15}{8} e^4 + \frac{5}{64} e^6 \right. \\ & \left. - \frac{11}{18} (1 - e^2)^{3/2} \left(1 + \frac{3}{2} e^2 + \frac{1}{8} e^4 \right) \right], \text{ and} \\ \frac{d}{dt} \left(\frac{P}{1 \text{ day}} \right) = & -\frac{6}{7} B \left(\frac{P}{1 \text{ day}} \right)^{-13/3} \frac{1}{(1 - e^2)^{15/2}} \left[1 + \frac{31}{2} e^2 + \frac{255}{8} e^4 \right. \\ & \left. + \frac{185}{16} e^6 + \frac{25}{64} e^8 - (1 - e^2)^{3/2} \left(1 + \frac{15}{2} e^2 + \frac{45}{8} e^4 + \frac{5}{16} e^6 \right) \right]. \end{aligned} \quad (6)$$

We chose the constant B to control the circularization efficacy over the binary lifetime, which we define as going from $t = 0$ to $t = 1$, where t is unitless.

Note that we ignore the changes in the stellar parameters, like radius and structure, and the stellar rotation, which must account for the varying angular momentum of the orbital motion. Furthermore, equations 6 are a simplified version of the actual tidal interaction, neglecting the dependence on the binary mass ratio, for example. Nevertheless, they are good enough for our purpose here (see, for example, the discussion of Terquem 2021).

We note that if we keep only the leading order of the eccentricity

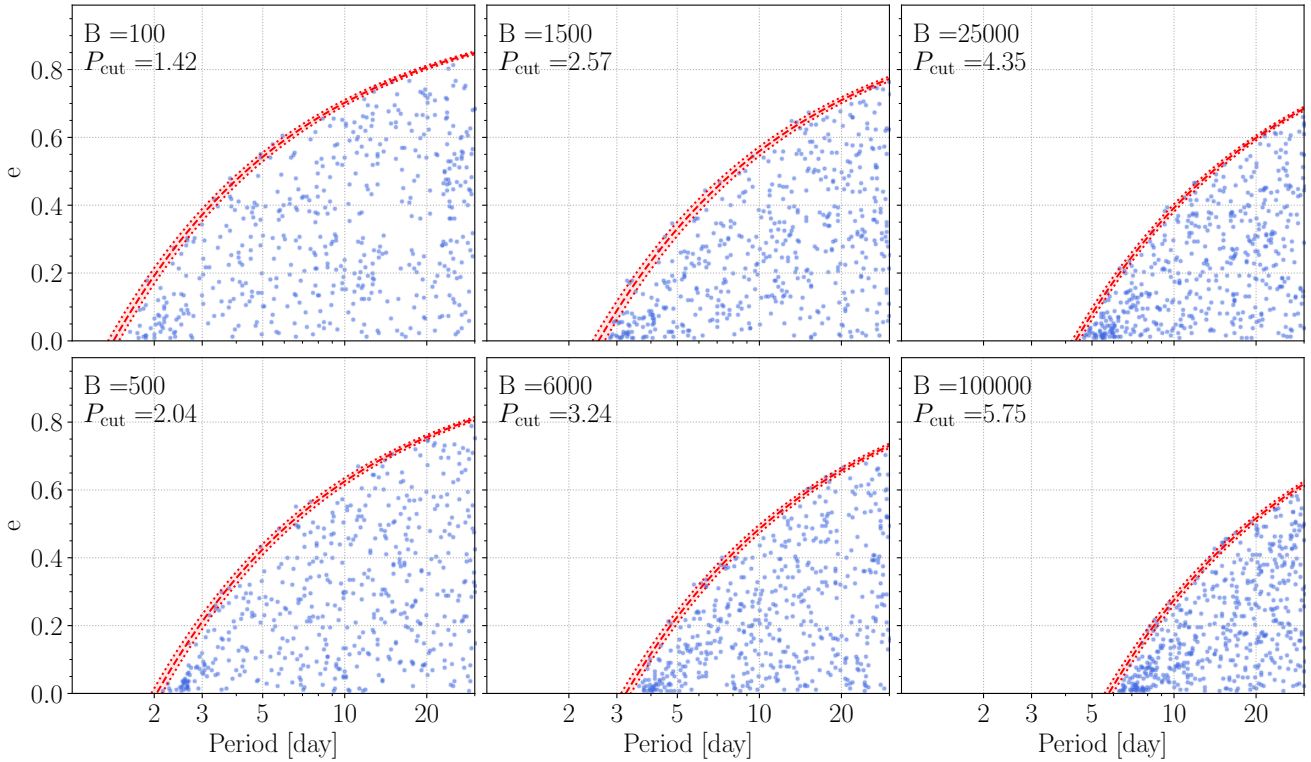


Figure 7. Simulated binary samples of 500 binaries each that were integrated through the circularization process following equations 8. The red lines show the upper envelopes, while the red area marks the transition region of $\pm\delta$ width along the envelope.

Table 1. Best-fitted values for P_{cut} , τ , δ of our simulated binary sample of 500 binaries for six bins of circularization parameter B

B	P_{cut} [day]	τ	δ
100	1.42 ± 0.05	1.61 ± 0.05	0.020 ± 0.007
500	2.04 ± 0.05	1.62 ± 0.04	0.020 ± 0.005
1500	2.57 ± 0.07	1.66 ± 0.04	0.022 ± 0.005
6000	3.24 ± 0.08	1.70 ± 0.05	0.018 ± 0.005
25000	4.35 ± 0.08	1.67 ± 0.04	0.013 ± 0.003
100000	5.75 ± 0.12	1.72 ± 0.05	0.015 ± 0.004

in equations 6 (i.e., $e \ll 1$), we get:

$$\frac{de}{dt} = -eB \left(\frac{P}{1 \text{ day}} \right)^{-16/3}, \text{ and} \quad (7)$$

$$\frac{d}{dt} \left(\frac{P}{1 \text{ day}} \right) = -\frac{57}{7} e^2 B \left(\frac{P}{1 \text{ day}} \right)^{-13/3}.$$

The approximated equations allow one to derive the eccentricity as a function of the period for a given binary

$$\ln(P/P_0) = \frac{57}{14} (e^2 - e_0^2), \quad (8)$$

where P_0 and e_0 are the period and eccentricity at the starting point of the circularization track. This equation does not predict the amount of change the eccentricity and period will go through in a given timespan but instead draws an evolutionary trajectory in the $(\log P, e)$ plane.

Table 1, as well as the six panels of Fig. 7, present the results of the integration through the "lifetime" of the samples, for six different

values of the circularization parameter, or alternatively for different lifetimes; these values span a range of three orders of magnitudes. Each sample contains 500 binaries of the same lifetime and circularization effectiveness B . Other simulations, not shown in the figure, showed that the best-fit obtained parameters do not depend on the number of binaries in the sample; only the uncertainties of the parameters do.

The panels clearly show that the separation between the circular and eccentric orbit is not a straight line but has a curved shape, supporting our approach that uses an upper envelope to characterize the period-eccentricity relation. Those envelopes are included in the figure, together with their corresponding cutoff periods.

The relation between the cutoff period P_{cut} and the circularization parameter B is presented in Fig. 8 by a tight linear relation, $\log P_{\text{cut}} = (0.198 \pm 0.011) \log(B) - (0.231 \pm 0.042)$, implying that

$$P_{\text{cut}} \propto B^{3/16}. \quad (9)$$

This can be traced back to equations 7 by noting that for small eccentricity the logarithmic derivative of e is approximated by $\frac{1}{e} \frac{de}{dt} \propto BP^{-16/3}$. P_{cut} is the period for which $\frac{\Delta e}{e} \sim 1$ during the "lifetime" of the binary, so that $BP_{\text{cut}}^{-16/3} \sim 1$.

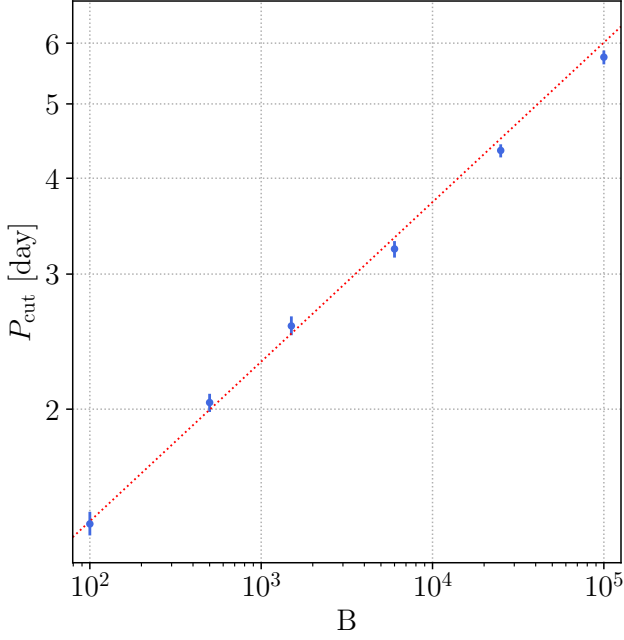


Figure 8. P_{cut} as function tidal dissipation effectiveness B for six simulated samples. Red-dotted line, $\log P_{\text{cut}} = (0.198 \pm 0.011) \log(B) - (0.231 \pm 0.042)$, marks the best-fit linear model.

5 CUTOFF PERIOD VS. EFFECTIVE TEMPERATURE IN MS BINARIES

The large number of *Gaia* MS binaries at hand enables us to look for the dependence of the cutoff period on the stellar temperature, which is readily available for most binaries. Fig. 9 shows a histogram of stellar temperatures of the 4376 orbits we have at hand (see above). We proceeded with the 3959 binaries in the range 5300 – 7700 K.

We divided those binaries into 18 temperature bins and fitted an upper envelope to each sub-sample with the our algorithm. We show in Fig. 10 the upper envelope best-fit model (red curve) and transition region of $\pm\delta$ width along the envelope (red area) of these binary samples. The results are summarized in Table 2 and Fig. 11, where the points and error bars mark our median and 16%, 84% percentiles.

The figure and the table offer a few features.

- P_{cut} drops linearity from ~ 6.5 day to ~ 2.5 day when moving from T_{eff} of 5500 to 6800.
- The linear model for the 13 bins is

$$\frac{P_{\text{cut}}}{\text{day}} = A + B \left(\frac{T_{\text{eff}}}{1000\text{K}} \right), \quad (10)$$

where $A = 27.6 \pm 2.5$ and $B = -3.69 \pm 0.39$.

- The linear fit is quite tight, suggesting that the uncertainties in P_{cut} are overestimated by a factor of ~ 1.7 . This could be expected, as the typical uncertainty in T_{eff} is of the same order as the bin width we used, inserting extra noise into the bins.

– P_{cut} is flat at the 7700 – 6800 K range (~ 3 day), and might be also flat at 5600 – 5300 K.

– A possible small jump of P_{cut} might be seen at the Kraft (1967) break of 6100 K.

– There is a strong correlation between P_{cut} and τ of the 18 bins — the shorter P_{cut} the larger τ is. This reflects the fact that the shape of the different upper envelopes is such that all reach the same

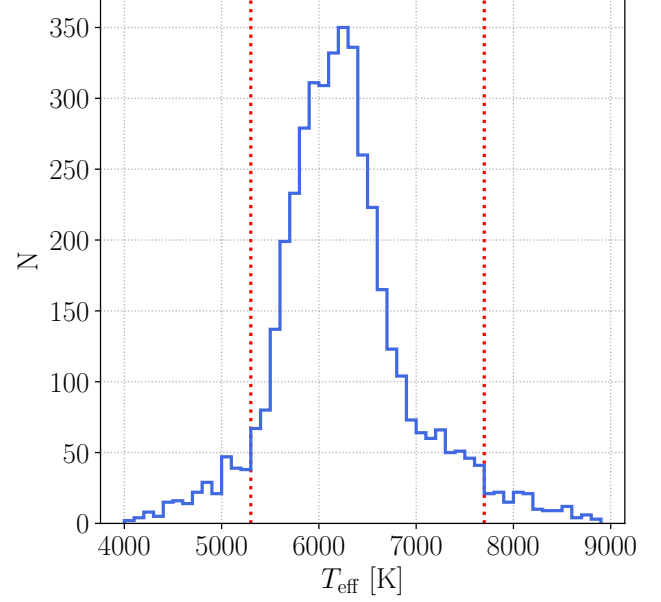


Figure 9. Stellar effective temperature histograms of our non-circular MS, $P < 30$ day, binary sample. Inside the range marked by red vertical dotted lines ($T_{\text{eff}} = 5300 - 7700$) there are 3959 binaries.

Table 2. Best-fitted values of P_{cut} , τ , δ for 18 temperature bins of the *Gaia* MS spectroscopic binaries.

T_{eff} [k]	N	P_{cut} [day]	τ	δ
5300 – 5500	148	7.00 ± 0.77	1.42 ± 0.16	0.08 ± 0.01
5500 – 5600	137	7.19 ± 0.86	1.37 ± 0.17	0.10 ± 0.02
5600 – 5700	198	6.57 ± 0.68	1.52 ± 0.14	0.08 ± 0.01
5700 – 5800	237	6.16 ± 0.49	1.40 ± 0.11	0.07 ± 0.01
5800 – 5900	280	6.52 ± 0.63	1.52 ± 0.12	0.09 ± 0.01
5900 – 6000	310	5.90 ± 0.47	1.50 ± 0.11	0.07 ± 0.01
6000 – 6100	307	5.44 ± 0.41	1.49 ± 0.11	0.08 ± 0.01
6100 – 6200	334	4.58 ± 0.32	1.76 ± 0.11	0.07 ± 0.01
6200 – 6300	348	4.52 ± 0.34	1.67 ± 0.11	0.07 ± 0.01
6300 – 6400	336	3.95 ± 0.40	1.83 ± 0.13	0.09 ± 0.01
6400 – 6500	261	4.22 ± 0.43	1.77 ± 0.14	0.09 ± 0.01
6500 – 6600	222	3.39 ± 0.44	1.91 ± 0.17	0.10 ± 0.02
6600 – 6700	165	3.19 ± 0.46	1.91 ± 0.22	0.09 ± 0.02
6700 – 6800	123	2.55 ± 0.41	2.26 ± 0.23	0.08 ± 0.03
6800 – 6900	104	2.90 ± 0.63	1.98 ± 0.24	0.11 ± 0.03
6900 – 7100	136	2.94 ± 0.38	1.95 ± 0.20	0.08 ± 0.02
7100 – 7300	126	3.46 ± 0.43	1.84 ± 0.20	0.08 ± 0.02
7300 – 7700	187	3.28 ± 0.38	1.87 ± 0.16	0.09 ± 0.01

eccentricity at a period of ~ 30 day. This can be explained by the fact that binaries with such relatively long periods retain their primordial eccentricities and therefore do not show any dependence on T_{eff} .

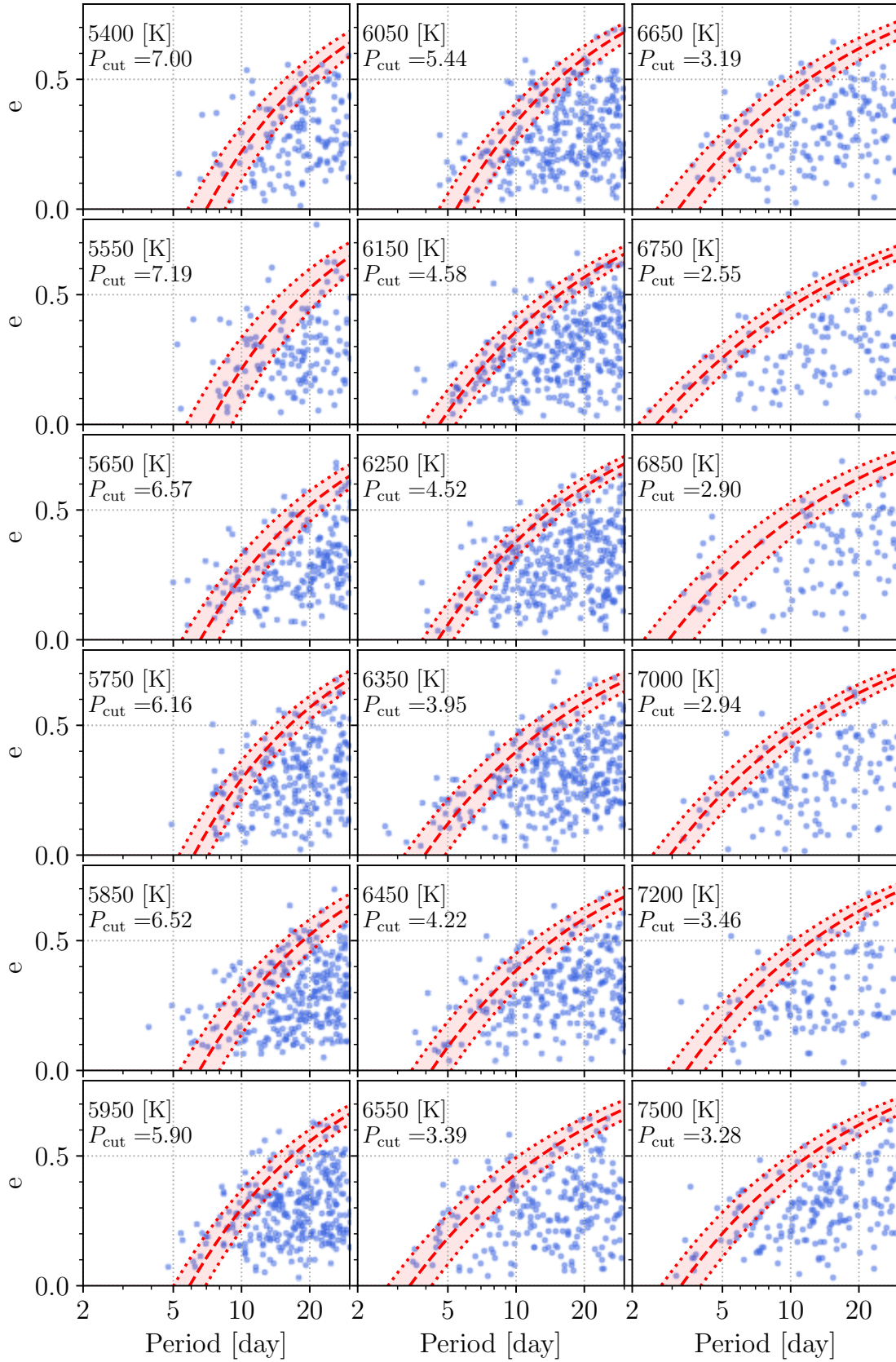


Figure 10. Period-eccentricity diagram with fitted upper envelope (see Table 2 for details) in red dashed line for the 18 sub-samples of the MS *Gaia* binaries. The red area marks the transition region of $\pm\delta$ along the envelope.

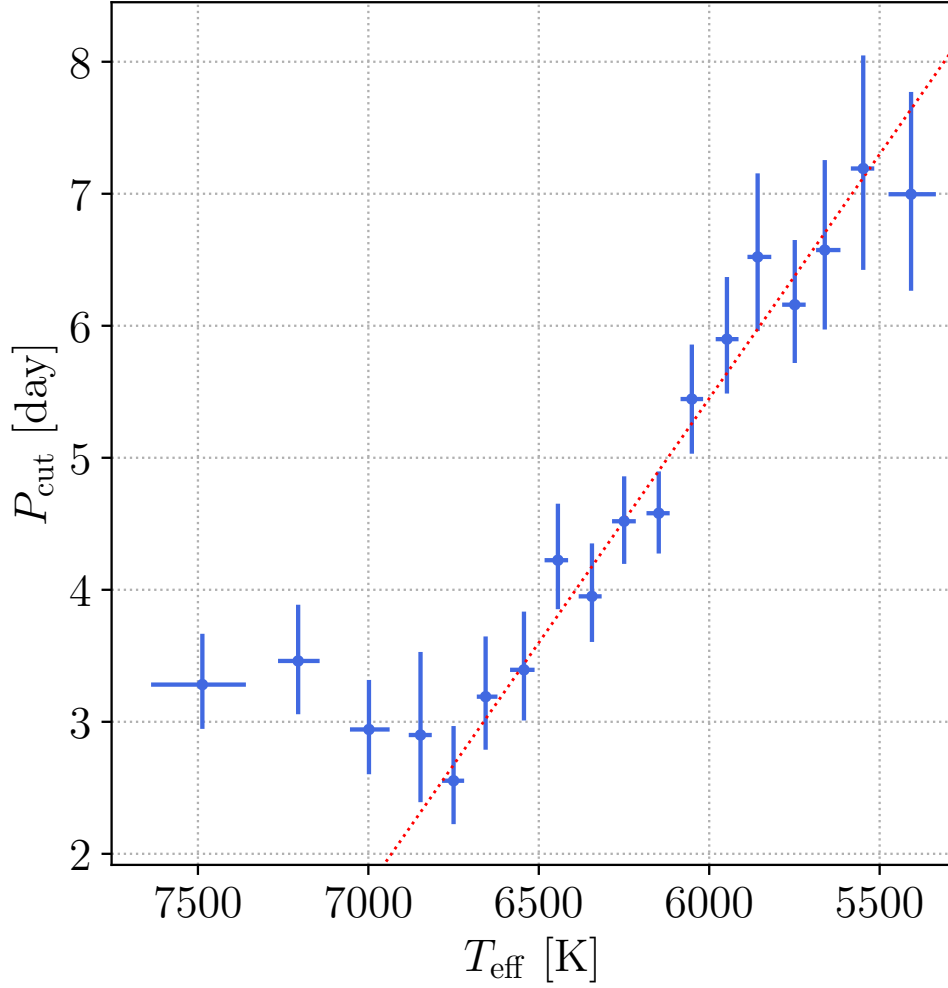


Figure 11. P_{cut} of 18 *Gaia* sub-samples as a function of their corresponding temperature. Red-dotted line, $P_{\text{cut}} = -3.69 (\pm 0.39) (T_{\text{eff}}/1000\text{K}) + 27.6 (\pm 2.5)$ day, marks the best-fit linear model ignoring the rightmost and four leftmost bins.

5.1 Cutoff period dependence on stellar age?

As shown in Fig. 5, the MS *Gaia* binaries show a strong correlation between stellar temperature and age. In this sub-section we examine the dependence of P_{cut} on both stellar parameters and show that the dependence on age, is weak if existing at all.

We divided the age-temperature plane into evenly spaced bins of 250 K and 2 Gyr, and derived P_{cut} for the 14 bins that contain more than 50 binaries. These P_{cut} values are colour coded in Fig. 12.

We fitted to the 14 bins a two-dimensional function of

$$\frac{P_{\text{cut}}}{\text{day}} = A_{2\text{D}} + B_{2\text{D}} \left(\frac{T_{\text{eff}}}{1000\text{K}} \right) + C_{2\text{D}} \left(\frac{\text{Age}}{\text{Gyr}} \right), \quad (11)$$

and ran an MCMC procedure to find the best values. We obtained $A_{2\text{D}} = 25.5 \pm 6.9$, $B_{2\text{D}} = -3.46 \pm 1.01$ and $C_{2\text{D}} = 0.08 \pm 0.11$.

This shows that P_{cut} strongly depends on stellar temperature and does not depend on the stellar age.

6 APPROXIMATED SCALING LAW OF CIRCULARIZATION

In this section, we try to scale the tidal interaction with the stellar mass and radius and the orbital period, in order to derive the theoretical

expectation for the dependence of P_{cut} on the stellar temperature and compare it to our observational results.

According to Zahn (1975, 1977); Zahn & Bouchet (1989); Zahn (1989) and Zahn (2008), the timescale of the circularization is determined by the turbulent dissipation, in cool stars with convective envelopes, and radiative damping, in hotter stars with radiative envelopes. We consider here the circularization of stars with radiative envelopes only, as at least half of the *Gaia* binaries analyzed here are of that type.

In a very simplified way, we consider only the eccentricity decay and ignore the period change associated with it. This can be close to reality only when the eccentricity is relatively small. Nevertheless, this approximation is probably good enough for the purpose of this section. The approximation of the eccentricity derivative, to first order in e , was already presented in equation 7

$$-\frac{1}{e} \frac{de}{dt} = B_{\text{rad}} P^{-7}, \quad (7)$$

where we follow the convention of Section 4. As emphasized there, changing the lifetime of a binary while keeping the circularization effectiveness is equivalent in our formulation to varying instead the B_{rad} parameter by the same factor.

Using Claret & Cunha (1997) equation 18 (see also Van Eylen

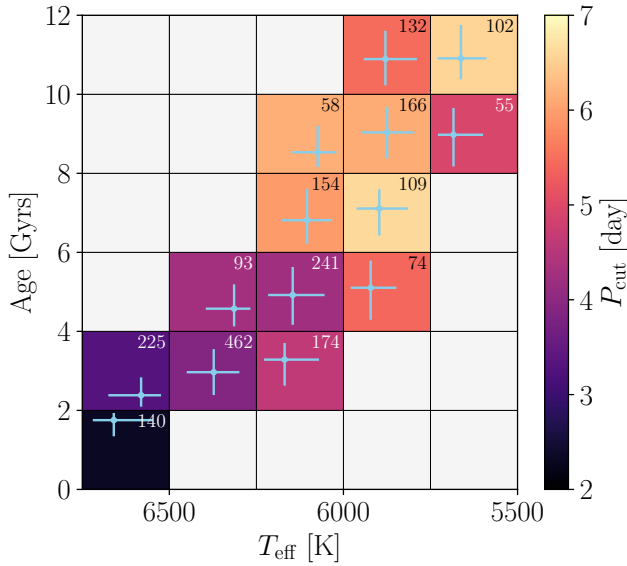


Figure 12. 2D histogram in evenly spaced bins of effective temperature and age. Colour represents P_{cut} of *Gaia* binaries in bins with more than 50 sources (otherwise white). Grey crosses mark median and 16%, 84% percentiles in each bin. The number of sources in each bin is displayed on the bin's top right side.

et al. 2016, equation 3), we write

$$B_{\text{rad}} \propto \frac{R_*^9}{M_*^3} \mathcal{F}(q) E_2 T_{\text{MS}}, \quad (12)$$

where $\mathcal{F}(q) = q/(1+q)^{5/3}$ is a function of the mass ratio, E_2 is a tidal constant evaluated numerically and T_{MS} is the MS lifetime. Adopting Van Eylen et al. (2016) scaling of $R_* \propto M_*^{0.8}$ and $T_{\text{MS}} \propto M_*^{-2.9}$, assuming the observed-stars age is a substantial fraction of their MS lifetime, we get

$$B_{\text{rad}} \propto M_*^{1.3} \mathcal{F}(q) E_2, \quad (13)$$

Using equation 43 of Hurley et al. (2002), $E_2 \propto M_*^{2.8}$, we finally get

$$B_{\text{rad}} \propto M_*^{4.1} \mathcal{F}(q), \quad (14)$$

indicating that B_{rad} is a monotonic *increasing* function of stellar mass, and consequently of stellar temperature.

Following Fig. 8 and Equation 9, we conclude that for radiative-envelope primaries $P_{\text{cut}} \propto B_{\text{rad}}^{1/7}$ and therefore

$$P_{\text{cut}} \propto M_*^{0.6}. \quad (15)$$

This implies that P_{cut} should also increase with stellar temperature, clearly in contrast with our results that show that P_{cut} is *decreasing with stellar temperature (or mass)* in the range of 5500 - 6700 K.

7 DISCUSSION

We used the cleaned *Gaia* sample of spectroscopic binaries to study the distribution of the orbital eccentricity as a function of the binary period. The distribution is characterized by an upper envelope (Poubaix et al. 2007; Mazeh 2008) that starts at P_{cut} and eccentricity zero and rises monotonically toward high eccentricities for longer periods. The assumption is that circularization processes induced by

tidal interaction between the two stars shaped the eccentricity distribution. The *Gaia* sample is a new opportunity to confront the theory of circularization with fresh data.

We model the upper envelope by a simple function of two parameters, one of which is P_{cut} , while the other, τ , determines the rise of the envelope. We then follow the Mazeh et al. (2016) approach and use a modified Fermi function to describe a probability density distribution of the binaries above and below the upper envelope in the $(\log P, e)$ plane. The probability density function converges to zero above the envelope, and to a positive constant below it, with a transition region of a derived width. We use an MCMC routine to find the best parameters of the distribution, given a sample of orbits.

The unprecedentedly large sample of *Gaia* orbits with MS A-, F- and G-type primaries enables us to derive the dependence of the envelope, and P_{cut} in particular, on the stellar temperature in the range of 5500 – 7500 K. To do that we divide the binaries into sub-samples of different temperatures, and fit the envelope of each sub-sample independently.

Our main finding is that P_{cut} presents a *linearly* decreasing function of stellar temperature for the G and F stars — from 6.5 day for 5700 K to ~ 2.5 day for $T_{\text{eff}} \sim 6800$ K, at a rate of -3.7 days/1000 K. The linear slope is at more than 9σ significance.

The uncertainties of the different P_{cut} values are larger than the scatter around the linear fit. We suggest these are due to "imperfections" of the samples, the result of different primordial eccentricity and period distributions, binaries with different ages and mass ratios, and stellar temperature spread, as the T_{eff} uncertainties are probably on the order of 100 K. It is quite surprising that, nevertheless, the linear dependence of P_{cut} is so pronounced and tight over a range of temperatures that correspond to stellar envelopes of convective and radiative nature alike.

In addition, P_{cut} is probably flat for T_{eff} at 5500 – 5700 K, and 6800 – 7500 K. At the well-known stellar Kraft brake of ~ 6100 K (see Kraft 1967) we possibly see a small jump, yet this is still barely significant.

We do not see any reason to believe our results are due to some *Gaia* observational bias. For example, we could not find any dependence of the quality score of Bashi et al. (2022), which estimates the degree of validity of the orbits, on stellar temperatures or orbital periods and eccentricities.

As we have shown, the P_{cut} trend revealed for the G- and F-stars is inconsistent with Zahn's circularization theory, when we assume that circularization took place during the stellar MS lifetime. This inconsistency could indicate that

- Zahn dynamical tide theory is not accurate enough to account for the circularization processes. An assertion of studies suggested different approaches (e.g., Alexander 1973; Hut 1981; Tassoul 1987; Hut et al. 1992; Dolginov & Smel'Chakova 1992; Goldman & Mazeh 1991, 1994; Goldman 2008; Witte & Savonije 1999, 2001, 2002; Duguid et al. 2020; Zanazzi & Wu 2021; Terquem 2021; Terquem & Martin 2021; Koenigsberger et al. 2021; Zanazzi 2022; Barker 2022; Preece et al. 2022; Wei 2022), in stars with radiative envelopes in particular; see, for example, a heated discussion between Tassoul & Tassoul (1997) and Rieutord (1992) and Rieutord & Zahn (1997), or
- The eccentricity distribution of the binaries was determined during the pre-main-sequence (PMS) phase of these stars, when the stars were much larger and therefore the circularization processes much faster, as suggested by Mayor & Mermilliod (1984), and worked out by Zahn & Bouchet (1989) and later by Khaliullin & Khaliullina (2011, KK11), using updated PMS models; see also Terquem & Martin (2021).

The latter conjecture is interesting, especially because it is coming from Zahn himself. Zahn & Bouchet (1989) claimed that for masses of $0.5 - 1.25 M_{\odot}$, the circularization took place during the PMS phase with expected P_{cut} between 7.2 and 8.5 day (see some observational evidence by Mathieu et al. 1992; Mathieu 1994; Melo et al. 2001). In fact, assuming the circularization occurred during the PMS phase, KK11 published a series of expected P_{cut} for different stellar masses based on updated PMS evolutionary tracks. Although the tracks are prone to a few uncertainties, the table of KK11 displays a trend that might be similar to our results — P_{cut} decreases as a function of the primary mass.

Understanding the theory of tidal circularization is crucial for understanding the evolution of short-period binaries (e.g., Hurley et al. 2002; Fragos et al. 2023). This has deep impact on how we think short-period binaries (e.g., Fabrycky & Tremaine 2007), close triple systems (Mazeh & Shaham 1979; Naoz 2016; Toonen et al. 2022), cataclysmic binaries (e.g., Patterson 1984) and X-ray binaries (e.g., Bildsten & Cutler 1992; Podsiadlowski et al. 2002) have evolved. Even some of the black-hole merger models depend on tidal interaction (e.g., Antonini et al. 2017; Belczynski et al. 2002).

Finally, tidal interaction could have a crucial role in the formation and evolution of exoplanets (Gu et al. 2003; Ida & Lin 2004; Ogilvie & Lin 2004; Terquem & Papaloizou 2007; Jackson et al. 2008; Rao et al. 2018), hot Jupiters (e.g., Rasio et al. 1996; Wu 2005; Ferraz-Mello et al. 2008; Leconte et al. 2010; Dawson & Johnson 2018) and their orbit alignment with the stellar spin (Dobbs-Dixon et al. 2004; Winn & Holman 2005; Fabrycky & Winn 2009; Scherrer et al. 2010; Lai 2012; Albrecht et al. 2012; Dawson 2014; Mazeh et al. 2015; Albrecht et al. 2021, 2022) in particular.

In the future, five observational avenues might be of use in order to deepen our understanding of the tidal interaction in binary systems. First, one can use other samples of spectroscopic binaries, to confirm our results and to find the dependence of P_{cut} on other parameters, like the mass ratio, stellar age and metallicity. Such samples include, for example, the next planned *Gaia* release,³ and results of multi-object spectrographs, like RAVE (Matijević et al. 2011), LAMOST (Cui et al. 2012), APOGEE (Price-Whelan et al. 2020) and the near-future 4MOST (de Jong et al. 2019).

The second avenue, analyzing samples of eclipsing binaries, was already taken by North & Zahn (2003); Mazeh et al. (2006); Van Eylen et al. (2016) and Justesen & Albrecht (2021), as detailed in the introduction. The advantage of using EBs is the capability to accurately derive small eccentricities, which is not possible for SB1s. It would be interesting to use additional samples, like that of *Gaia* (Mowlavi et al. 2022) and derive P_{cut} as a function of T_{eff} . The large photometric surveys at work, like ZTF (Chen et al. 2020) and ASAS-SN (Paczynski et al. 2006; Rowan et al. 2022) can yield large samples of additional eclipsing binaries.

The third avenue has to do with the obvious realization that the long-term tidal interaction is not limited to circularization but acts to synchronize (see Khaliullin & Khaliullina 2010) and align the binary with the stellar rotation (e.g., Hurley et al. 2002; Naoz & Fabrycky 2014). Therefore, a sample of binaries should also display synchronization and alignment cutoff periods. It would be interesting if we could compare those periods with the circularization period and their dependence on stellar parameters.

To follow the stellar rotation one can use the available large set of photometric light curves, like those of OGLE (e.g., Soszyński et al. 2016), *TESS* (Huang et al. 2020) and *Gaia* (Eyer et al. 2022), which

can reveal the stellar rotation periods (McQuillan et al. 2013, 2014; Avallone et al. 2022). Synchronization can be assumed, for example, if one detects ellipsoidal variability, which is modulated with the binary period (Faigler & Mazeh 2011; Faigler et al. 2012; Green et al. 2022).

The fourth avenue has to do with observed eccentric pseudosynchronized binaries (Hut 1981), discovered in the *Kepler* lightcurves (e.g., Zimmerman et al. 2017; Saio & Kurtz 2022), which are going through strong tidal interaction. It would be interesting to compare their stellar rotation periods with the tidal theory expectation. In one of these systems, an orbital-period decay driven by tidal interaction has been probably observed (Ou et al. 2021).

Finally, recently some observational evidence has been presented for the orbital decay of very close hot Jupiters, like WASP-12 (e.g., Yee et al. 2020; Turner et al. 2021; Wong et al. 2022); see also Harre et al. (2023), Yang & Wei (2022) and Rosário et al. (2022), based on the precise timings of transits that span over more than a decade. Following the planetary period decay in real time (Yang et al. 2022) has the exciting potential to further constrain the theory of tidal interaction.

When additional information is available, the observational evidence could be compared with a more realistic tidal model that might be combined with some conjecture about the primordial period-eccentricity distribution. Such a model may include other evolutionary mechanisms, like magnetic breaking (e.g., Mestel 1968; Fleming et al. 2019) and interaction with accretion discs and/or third companions (e.g., Fabrycky & Tremaine 2007; Naoz 2016; Toonen et al. 2022), so it can account for the observed statistical features of the population of short-period binaries.

ACKNOWLEDGEMENTS

We are deeply indebted to the *NSS* group and all the *Gaia* team for producing a vast high-quality catalogue that enabled us to follow the tidal circularization of short-period binaries. We are extremely grateful to Josh N. Winn and Robert D. Mathieu for their illuminating comments and wise suggestions that have significantly improved this manuscript. The referee contributed very helpful comments on a previous version of the paper, helping us presenting our results in a clearer way. This research was supported by Grant No. 2016069 of the United States-Israel Binational Science Foundation (BSF) to TM, and Grant No. I-1498-303.7/2019 of the German-Israeli Foundation for Scientific Research and Development (GIF) to TM. This work has also made use of data from the European Space Agency (ESA) mission *Gaia* (<https://www.cosmos.esa.int/gaia>), processed by the *Gaia* Data Processing and Analysis Consortium (DPAC; <https://www.cosmos.esa.int/web/gaia/dpac/consortium>). Funding for DPAC has been provided by national institutions, in particular the institutions participating in the *Gaia* Multilateral Agreement.

DATA AVAILABILITY

Data used in this study are available upon request from the corresponding author.

REFERENCES

- Albrecht S., et al., 2012, *ApJ*, 757, 18
 Albrecht S. H., Marcussen M. L., Winn J. N., Dawson R. I., Knudstrup E., 2021, *ApJ*, 916, L1

³ <https://www.cosmos.esa.int/web/gaia/release>

- Albrecht S. H., Dawson R. I., Winn J. N., 2022, *PASP*, **134**, 082001
- Alexander M. E., 1973, *Ap&SS*, **23**, 459
- Antonini F., Toonen S., Hamers A. S., 2017, *ApJ*, **841**, 77
- Avallone E. A., et al., 2022, *ApJ*, **930**, 7
- Barker A. J., 2022, *ApJ*, **927**, L36
- Bashi D., Shahaf S., Mazeh T., Faigler S., Dong S., El-Badry K., Rix H. W., Jorissen A., 2022, *MNRAS*, **517**, 3888
- Belczynski K., Kalogera V., Bulik T., 2002, *ApJ*, **572**, 407
- Bildsten L., Cutler C., 1992, *ApJ*, **400**, 175
- Blomme R., et al., 2022, arXiv e-prints, p. arXiv:2206.05486
- Boffin H. M. J., 2012, in Arenou F., Hestroffer D., eds, *Orbital Couples: Pas de Deux in the Solar System and the Milky Way*. pp 41–44
- Boffin H. M. J., 2015, *A&A*, **575**, L13
- Chen X., Wang S., Deng L., de Grijs R., Yang M., Tian H., 2020, *ApJS*, **249**, 18
- Claret A., Cunha N. C. S., 1997, *A&A*, **318**, 187
- Cui X.-Q., et al., 2012, *RAA*, **12**, 1197
- Dawson R. I., 2014, *ApJ*, **790**, L31
- Dawson R. I., Johnson J. A., 2018, *ARA&A*, **56**, 175
- Dobbs-Dixon I., Lin D. N. C., Mardling R. A., 2004, *ApJ*, **610**, 464
- Dolginov A. Z., Smel'Chakova E. V., 1992, *A&A*, **257**, 783
- Duchêne G., Kraus A., 2013, *ARA&A*, **51**, 269
- Duguid C. D., Barker A. J., Jones C. A., 2020, *MNRAS*, **491**, 923
- Duquennoy A., Mayor M., 1991, *A&A*, **248**, 485
- Eyer L., et al., 2022, arXiv e-prints, p. arXiv:2206.06416
- Fabrycky D., Tremaine S., 2007, *ApJ*, **669**, 1298
- Fabrycky D. C., Winn J. N., 2009, *ApJ*, **696**, 1230
- Faigler S., Mazeh T., 2011, *MNRAS*, **415**, 3921
- Faigler S., Mazeh T., Quinn S. N., Latham D. W., Tal-Or L., 2012, *ApJ*, **746**, 185
- Ferraz-Mello S., Rodríguez A., Hussmann H., 2008, *Celestial Mechanics and Dynamical Astronomy*, **101**, 171
- Fleming D. P., Barnes R., Davenport J. R. A., Luger R., 2019, *ApJ*, **881**, 88
- Foreman-Mackey D., et al., 2013, emcee: The MCMC Hammer, *Astrophysics Source Code Library* (ascl:1303.002)
- Fragos T., et al., 2023, *ApJS*, **264**, 45
- Gaia Collaboration et al., 2022, arXiv e-prints, p. arXiv:2206.05595
- Geller A. M., Mathieu R. D., 2012, *AJ*, **144**, 54
- Geller A. M., Mathieu R. D., Harris H. C., McClure R. D., 2008, *AJ*, **135**, 2264
- Geller A. M., Mathieu R. D., Braden E. K., Meibom S., Platais I., Dolan C. J., 2010, *AJ*, **139**, 1383
- Geller A. M., Mathieu R. D., Latham D. W., Pollack M., Torres G., Leiner E. M., 2021, *AJ*, **161**, 190
- Giuricin G., Mardirossian F., Mezzetti M., 1984, *A&A*, **134**, 365
- Goldman I., 2008, *Astronomische Nachrichten*, **329**, 762
- Goldman I., Mazeh T., 1991, *ApJ*, **376**, 260
- Goldman I., Mazeh T., 1994, *ApJ*, **429**, 362
- Green M. J., Maoz D., Mazeh T., Faigler S., Shahaf S., Gommel R., El-Badry K., Rix H.-W., 2022, arXiv e-prints, p. arXiv:2211.06194
- Gu P.-G., Lin D. N. C., Bodenheimer P. H., 2003, *ApJ*, **588**, 509
- Hara N. C., Boué G., Laskar J., Delisle J. B., Unger N., 2019, *MNRAS*, **489**, 738
- Harre J. V., et al., 2023, *A&A*, **669**, A124
- Huang C. X., et al., 2020, *Research Notes of the American Astronomical Society*, **4**, 204
- Hurley J. R., Tout C. A., Pols O. R., 2002, *MNRAS*, **329**, 897
- Hut P., 1981, *A&A*, **99**, 126
- Hut P., et al., 1992, *PASP*, **104**, 981
- Ida S., Lin D. N. C., 2004, *ApJ*, **604**, 388
- Jackson B., Greenberg R., Barnes R., 2008, *ApJ*, **678**, 1396
- Jha S., Torres G., Stefanik R. P., Latham D. W., Mazeh T., 2000, *MNRAS*, **317**, 375
- Justesen A. B., Albrecht S., 2021, *ApJ*, **912**, 123
- Katz D., et al., 2022, arXiv e-prints, p. arXiv:2206.05902
- Khaliullin K. F., Khaliullina A. I., 2010, *MNRAS*, **401**, 257
- Khaliullin K. F., Khaliullina A. I., 2011, *MNRAS*, **411**, 2804
- Koenigsberger G., Moreno E., Langer N., 2021, *A&A*, **653**, A127
- Kopal Z., 1956, *Annales d'Astrophysique*, **19**, 298
- Kraft R. P., 1967, *ApJ*, **150**, 551
- Lai D., 2012, *MNRAS*, **423**, 486
- Leconte J., Chabrier G., Baraffe I., Levrard B., 2010, *A&A*, **516**, A64
- Lucy L. B., Sweeney M. A., 1971, *AJ*, **76**, 544
- Mathieu R. D., 1994, *ARA&A*, **32**, 465
- Mathieu R. D., Mazeh T., 1988, *ApJ*, **326**, 256
- Mathieu R. D., Latham D. W., Mazeh T., Duquennoy A., Mayor M., Mermilliod J. C., 1992, in *Binaries as Tracers of Star Formation*. pp 278–290
- Mathieu R. D., Meibom S., Dolan C. J., 2004, *ApJ*, **602**, L121
- Matijević G., et al., 2011, *AJ*, **141**, 200
- Mayor M., Mermilliod J. C., 1984, in *Observational Tests of the Stellar Evolution Theory*. p. 411
- Mazeh T., 1990, *AJ*, **99**, 675
- Mazeh T., 2008, in Goupil M. J., Zahn J. P., eds, *EAS Publications Series Vol. 29, EAS Publications Series*. pp 1–65 (arXiv:0801.0134), doi:10.1051/eas:0829001
- Mazeh T., Goldberg D., 1992, *ApJ*, **394**, 592
- Mazeh T., Shaham J., 1979, *A&A*, **77**, 145
- Mazeh T., Tamuz O., North P., 2006, *MNRAS*, **367**, 1531
- Mazeh T., Perets H. B., McQuillan A., Goldstein E. S., 2015, *ApJ*, **801**, 3
- Mazeh T., Holczer T., Faigler S., 2016, *A&A*, **589**, A75
- McQuillan A., Aigrain S., Mazeh T., 2013, *MNRAS*, **432**, 1203
- McQuillan A., Mazeh T., Aigrain S., 2014, *ApJS*, **211**, 24
- Meibom S., Mathieu R. D., 2005, *ApJ*, **620**, 970
- Melo C. H. F., Covino E., Alcalá J. M., Torres G., 2001, *A&A*, **378**, 898
- Mestel L., 1968, *MNRAS*, **138**, 359
- Moe M., Di Stefano R., 2017, *ApJS*, **230**, 15
- Mowlavi N., et al., 2022, arXiv e-prints, p. arXiv:2211.00929
- Naoz S., 2016, *ARA&A*, **54**, 441
- Naoz S., Fabrycky D. C., 2014, *ApJ*, **793**, 137
- Nine A. C., Milliman K. E., Mathieu R. D., Geller A. M., Leiner E. M., Platais I., Tofflemire B. M., 2020, *AJ*, **160**, 169
- North P., Zahn J. P., 2003, *A&A*, **405**, 677
- Ogilvie G. I., Lin D. N. C., 2004, *ApJ*, **610**, 477
- Ou J.-W., Yu C., Jiang C., Yang M., Niu H., 2021, *MNRAS*, **508**, 3967
- Paczynski B., Szczygieł D. M., Pilecki B., Pojmański G., 2006, *MNRAS*, **368**, 1311
- Paegert M., Stassun K. G., Collins K. A., Pepper J., Torres G., Jenkins J., Twicken J. D., Latham D. W., 2021, arXiv e-prints, p. arXiv:2108.04778
- Patterson J., 1984, *ApJS*, **54**, 443
- Pedregosa F., et al., 2011, *Journal of Machine Learning Research*, **12**, 2825
- Podsiadlowski P., Rappaport S., Pfahl E. D., 2002, *ApJ*, **565**, 1107
- Pourbaix D., et al., 2007, *VizieR Online Data Catalog*, p. B/sb9
- Preece H. P., Hamers A. S., Neunteufel P. G., Schaefer A. L., Tout C. A., 2022, *ApJ*, **933**, 25
- Price-Whelan A. M., et al., 2020, *ApJ*, **895**, 2
- Raghavan D., et al., 2010, *ApJS*, **190**, 1
- Rao S., Meynet G., Eggenberger P., Haemmerlé L., Privitera G., Georgy C., Ekström S., Mordasini C., 2018, *A&A*, **618**, A18
- Rasio F. A., Tout C. A., Lubow S. H., Livio M., 1996, *ApJ*, **470**, 1187
- Recio-Blanco A., et al., 2022, arXiv e-prints, p. arXiv:2206.05541
- Ricker G. R., et al., 2015, *Journal of Astronomical Telescopes, Instruments, and Systems*, **1**, 014003
- Rieutord M., 1992, *A&A*, **259**, 581
- Rieutord M., Zahn J.-P., 1997, *ApJ*, **474**, 760
- Rosário N. M., Barros S. C. C., Demangeon O. D. S., Santos N. C., 2022, *A&A*, **668**, A114
- Rowan D. M., et al., 2022, *MNRAS*, **517**, 2190
- Saio H., Kurtz D. W., 2022, *MNRAS*, **511**, 560
- Scherrer R. J., Berlind A. A., Mao Q., McBride C. K., 2010, *ApJ*, **708**, L9
- Shahaf S., Mazeh T., Faigler S., 2017, *MNRAS*, **472**, 4497
- Slawson R. W., et al., 2011, *AJ*, **142**, 160
- Soszyński I., et al., 2016, *Acta Astron.*, **66**, 405
- Stassun K. G., et al., 2018, *AJ*, **156**, 102
- Sterne T. E., 1940, *Proceedings of the National Academy of Science*, **26**, 36
- Tassoul J.-L., 1987, *ApJ*, **322**, 856
- Tassoul M., Tassoul J.-L., 1997, *ApJ*, **481**, 363

- Terquem C., 2021, *MNRAS*, 503, 5789
- Terquem C., Martin S., 2021, *MNRAS*, 507, 4165
- Terquem C., Papaloizou J. C. B., 2007, *ApJ*, 654, 1110
- Toonen S., Boekholt T. C. N., Portegies Zwart S., 2022, *A&A*, 661, A61
- Torres G., Latham D. W., Quinn S. N., 2021, *ApJ*, 921, 117
- Troup N. W., et al., 2016, *AJ*, 151, 85
- Turner J. D., Ridden-Harper A., Jayawardhana R., 2021, *AJ*, 161, 72
- Van Eylen V., Winn J. N., Albrecht S., 2016, *ApJ*, 824, 15
- Wei X., 2022, *A&A*, 664, A10
- Winn J. N., Holman M. J., 2005, *ApJ*, 628, L159
- Witte M. G., Savonije G. J., 1999, *A&A*, 350, 129
- Witte M. G., Savonije G. J., 2001, *A&A*, 366, 840
- Witte M. G., Savonije G. J., 2002, *A&A*, 386, 222
- Wong I., Shporer A., Vissapragada S., Greklek-McKeon M., Knutson H. A., Winn J. N., Benneke B., 2022, *AJ*, 163, 175
- Wu Y., 2005, *ApJ*, 635, 688
- Wyrzykowski L., et al., 2003, *Acta Astron.*, 53, 1
- Yang F., Wei X., 2022, *PASP*, 134, 024401
- Yang F., et al., 2022, *Research in Astronomy and Astrophysics*, 22, 055005
- Yee S. W., et al., 2020, *ApJ*, 888, L5
- Zahn J. P., 1975, *A&A*, 41, 329
- Zahn J. P., 1977, *A&A*, 57, 383
- Zahn J. P., 1989, *A&A*, 220, 112
- Zahn J. P., 2008, in Goupil M. J., Zahn J. P., eds, *EAS Publications Series Vol. 29, EAS Publications Series*. pp 67–90 ([arXiv:0807.4870](https://arxiv.org/abs/0807.4870)), [doi:10.1051/eas:082900210.48550/arXiv.0807.4870](https://doi.org/10.1051/eas:082900210.48550/arXiv.0807.4870)
- Zahn J. P., Bouchet L., 1989, *A&A*, 223, 112
- Zanazzi J. J., 2022, *ApJ*, 929, L27
- Zanazzi J. J., Wu Y., 2021, *AJ*, 161, 263
- Zimmerman M. K., Thompson S. E., Mullally F., Fuller J., Shporer A., Hambleton K., 2017, *ApJ*, 846, 147
- de Jong R. S., et al., 2019, *The Messenger*, 175, 3

This paper has been typeset from a $\text{\TeX}/\text{\LaTeX}$ file prepared by the author.